Chemical Science

ROYAL SOCIETY OF CHEMISTRY

EDGE ARTICLE

View Article Online
View Journal | View Issue

Cite this: *Chem. Sci.*, 2025, **16**, 6434

All publication charges for this article have been paid for by the Royal Society of Chemistry

Enhancing electroluminescence performance of ultra-deep-blue through-space charge transfer emitters with $CIE_y \approx 0.05$ *via* methyl-modification†

Quanwei Li,[a] Haisong Zhao,[a] Jinyang Zhao,[a] Zhongxu Cao,[a] Chao Yu,[a] Shouke Yan *[ab] and Zhongjie Ren *[a]

Received 29th November 2024
Accepted 8th March 2025

DOI: 10.1039/d4sc08094g

rsc.li/chemical-science

Achieving efficient solution-processed ultra-deep-blue OLEDs remains a challenge. Herein, a methyl-modification strategy is proposed to overcome weak intramolecular charge transfer and the large energy gap between the singlet and triplet states (ΔE_{ST}) of ultra-deep-blue through-space charge transfer (TSCT)-thermally activated delayed fluorescence (TADF) emitters. In this way, the reverse intersystem crossing (RISC) process is found to be effective from T_1 to S_1 and can be accelerated with the assistance of T_2. As a result, the ultra-deep-blue TSCT emitter **3MeCz-BO** exhibits a minimized ΔE_{ST} of 0.02 eV, and an enhanced RISC rate of 3.71×10^5 s^{-1}. Additionally, this modification can improve the solubility, enabling the fabrication of solution-processed organic light-emitting diodes (OLEDs). The maximum external quantum efficiency of the **3MeCz-BO**-based solution-processed OLED reaches 10.1%, with a Commission Internationale de L'Eclairage (CIE) coordinates of (0.151, 0.051) and a luminance of 1334 cd m^{-2}. This work is the first instance of developing high-performance ultra-deep-blue solution-processed TSCT-TADF OLEDs, which show comparable performance to vacuum-deposited OLEDs. Furthermore, the **3MeCz-BO**-based OLED fits well within the standard Red Green Blue (sRGB) of CIE coordinates (0.15, 0.06), and is close to the CIE coordinates (0.131, 0.046) for the Rec. 2020 standard, implying its potential application in colorful display devices.

Introduction

Thermally activated delayed fluorescence (TADF) emitters represent the third generation of light-emitting materials for organic light-emitting diodes (OLEDs), achieving nearly 100% exciton utilization without any precious heavy metals.[1–3] Through-space charge transfer (TSCT) allows for the spatial separation of the highest occupied molecular orbital (HOMO) and the lowest unoccupied molecular orbital (LUMO), resulting in a small energy gap between singlet and triplet excited states (ΔE_{ST}).[4–7] In 2020, π-stacked molecules with space-confined face-to-face donors and acceptors were proposed by Jiang *et al.* to fabricate high-efficiency TSCT-TADF OLEDs.[8]

In recent years, high-performance TSCT-TADF materials have been widely developed and used in blue,[8–17] green,[18–27] and red[28–31] OLEDs. Although TSCT is advantageous for reducing the ΔE_{ST} of TADF materials, achieving a small ΔE_{ST} for deep-blue TSCT-TADF materials with $CIE_y \leq 0.1$ still remains challenging, due to weak intramolecular charge transfer (ICT). Therefore, it is hard to develop high-performance ultra-deep-blue TSCT-TADF materials. Oxygen-bridged boron was first reported for OLED materials[32] and has been widely utilized to fabricate deep-blue OLEDs.[33–36] Based on this, our group previously developed deep-blue TSCT materials, **QAc-BO** and **Cz-BO**, but they possess high ΔE_{ST} values of 0.20 and 0.29 eV.[13] The high ΔE_{ST} limits the performance of the OLEDs. Additionally, Zhao *et al.* developed violet TSCT materials with extremely low CIE_y (<0.03).[37] However, the significant ΔE_{ST} (≈0.3 eV) makes TADF characteristics nearly unnoticeable. For ultra-deep-blue TADF materials with low CIE_y, controlling ΔE_{ST} becomes increasingly difficult. Due to weak ICT, these materials generally display a large bandgap, resulting in a high-energy singlet charge transfer state (^{1}CT). The triplet charge transfer state (^{3}CT) is generally positioned near ^{1}CT, with both states residing at high energy levels. In contrast, the triplet local excited state (^{3}LE) is primarily determined by the molecular segment with the lowest energy, which could be the donor, the acceptor, or the bridge connecting them, and this state is typically much lower in energy than ^{3}CT. As a result, the ΔE_{ST} of these materials, mainly determined by ^{1}CT and ^{3}LE, tends to increase.[38–40]

[a]*State Key Laboratory of Chemical Resource Engineering, Beijing University of Chemical Technology, Beijing 100029, China. E-mail: renzj@mail.buct.edu.cn*

[b]*Department Key Laboratory of Rubber-Plastics Ministry of Education, School of Polymer Science and Engineering, Qingdao University of Science & Technology, Qingdao 266042, China*

† Electronic supplementary information (ESI) available. CCDC 2402467–2402469 contain the crystallographic data for **1MeCz-BO**, **2MeCz-BO** and **3MeCz-BO**. For ESI and crystallographic data in CIF or other electronic format see DOI: https://doi.org/10.1039/d4sc08094g

This challenges the reverse intersystem crossing (RISC) process in ultra-deep-blue TSCT-TADF materials.

To address the issue of large ΔE_{ST} in ultra-deep-blue TSCT-TADF materials, this work innovatively modified methyl groups at three positions in the donor; referring to the previously developed fluorescent material **Cz-BO**, three new TSCT-TADF materials were prepared: **1MeCz-BO**, **2MeCz-BO**, and **3MeCz-BO**. The molecular design concept is shown in Fig. 1. Due to the electron-rich nature of methyl groups, they can enhance ICT and thus reduce the energy levels of ^{1}CT and ^{3}CT, while ^{3}LE remains unaffected. This leads to a reduction in ΔE_{ST}. In addition, the energy gap between ^{3}CT and ^{3}LE ($\Delta E(^3\text{CT} - {}^3\text{LE})$) was also reduced, leading to the mixing and hybridization of ^{3}CT and ^{3}LE. Therefore, both T_1 and T_2 have certain LE characteristics. This could enhance the spin–orbit coupling (SOC) values of T_1–S_1 and T_2–S_1, allowing RISC to occur from T_1 and T_2 and to be accelerated with the assistance of T_2. In this methyl-modification design, the optimized **3MeCz-BO** shows ultra-deep-blue emission at 432 nm, achieving a small ΔE_{ST} of 0.02 eV and an enhanced RISC rate of 3.17×10^5 s^{-1}. Additionally, the methyl-modified TSCT-TADF materials show good solubility and are suitable for fabricating OLED devices by solution processing. As a result, the EQE_{max} of solution-processed **3MeCz-BO**-based OLEDs is 10.1%, with a full width at half maximum (FWHM) of 50 nm, and a high luminance of 1334 cd m^{-2}. Furthermore, the notable Commission Internationale de L'Eclairage (CIE) coordinates of **3MeCz-BO** (0.151, 0.051) fit well within the standard Red Green Blue (sRGB) of CIE coordinates (0.15, 0.06), and are close to the CIE coordinates (0.131, 0.046) for the Rec. 2020 standard. This suggests its potential application in colorful display devices.

Results and discussion

Synthesis and characterization

The chemical structures of **1MeCz-BO**, **2MeCz-BO**, and **3MeCz-BO** are shown in Fig. 1. The synthetic routes are provided in the ESI (Scheme S1†). The donor units consist of the 4-methylphenyl group (or without methyl group) and dimethyl-carbazole (or carbazole) by nucleophilic substitution reactions. Unlike **Cz-BO**,[13] the *tert*-butyl groups on the acceptors are replaced with methyl groups, to reduce the steric hindrance caused by *tert*-butyl groups and generate parallel D–A arrangements. The Suzuki–Miyaura cross-coupling reaction was performed to couple the acceptor and the bridge units to retain the intermediate compound **4**. The final emitters are prepared through lithium–bromine exchange of the donor and exchange reaction with compound **4**. The emitters show good solubility in organic solvents such as dichloromethane and chlorobenzene, owing to their external methyl groups. The chemical structures of all intermediates and final products were characterized by ^{1}H NMR, ^{13}C NMR, high-resolution mass spectrometry, and elemental analysis (Fig. S1–S19†).

To evaluate the thermal stabilities of **1MeCz-BO**, **2MeCz-BO**, and **3MeCz-BO**, their thermal decomposition temperatures (T_ds) were measured by thermogravimetric analysis (TGA) under a nitrogen atmosphere (Fig. S20†). The T_d values for 5% weight loss are 415 °C for **1MeCz-BO**, 413 °C for **2MeCz-BO**, and 412 °C for **3MeCz-BO**. The excellent thermal stability arises from the rigid molecules, which is beneficial for the fabrication of OLEDs. Cyclic voltammetry (CV) measurements were conducted to determine the oxidation–reduction potentials of the materials (Fig. S21a†). The HOMO values of **1MeCz-**

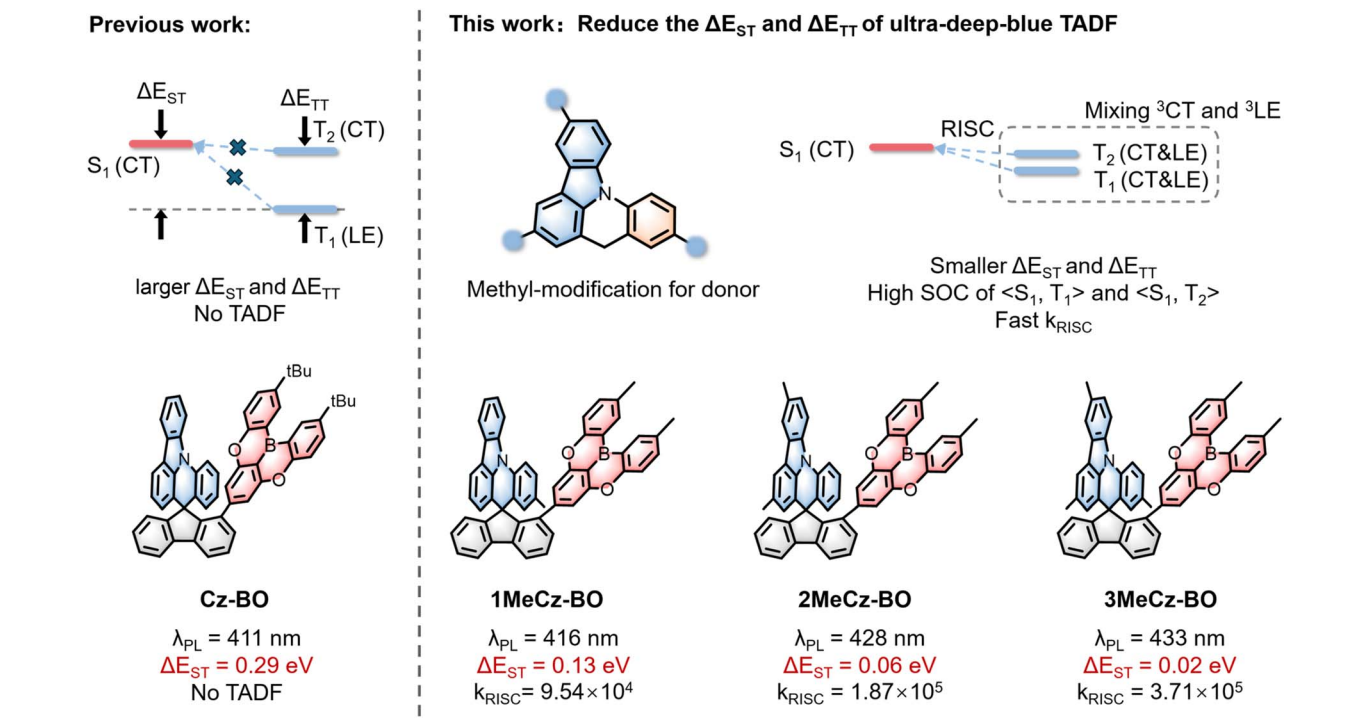

Fig. 1 Molecular design concept and the chemical structures of 1MeCz-BO, 2MeCz-BO, and 3MeCz-BO.

BO, **2MeCz-BO**, and **3MeCz-BO** are estimated to be −5.41, −5.29, and −5.23 eV, respectively. **1MeCz-BO** shows the deepest HOMO level, while **3MeCz-BO** shows the shallowest HOMO level, which results from the number of electronic-rich methyl groups. The LUMO values are measured as −2.85, −2.84, and −2.82 eV for **1MeCz-BO**, **2MeCz-BO**, and **3MeCz-BO**, respectively. The similar structure of their acceptors indicates similar LUMO energy levels.

The calculated HOMO–LUMO energy gap (E_g) values are 2.56, 2.45, and 2.41 eV, respectively, suggesting an enhanced ICT and slight redshift emission with the increase in the methyl groups on the donor. Moreover, the pseudo-reversible redox processes are validated by CV measurements over multiple cycles (Fig. S29b–d†), suggesting good device stability when charges are injected repeatedly into the emitter.

Single crystals and theoretical calculations

To unequivocally investigate the molecular spatial structure of the compounds, single crystals of **1MeCz-BO** (CCDC 2402467), **2MeCz-BO** (CCDC 2402468), and **3MeCz-BO** (CCDC 2402469) were obtained by slow evaporation from a mixture of dichloromethane and methanol (v/v = 1 : 4) at room temperature. The spatial structures were obtained from X-ray diffraction analysis, as shown in Fig. 2a and b from the side and top view. Besides this, X-ray crystallographic data are summarized in Table S1,† the packing modes in the single crystals of the compounds are shown in Fig. S22,† and the ORTEP diagrams of the compounds are shown in Fig. S23–S25.† To distinguish between the donor and acceptor units in different compounds, we designate the donors as D1, D2, and D3, and the acceptors as A1, A2, and A3, in **1MeCz-BO**, **2MeCz-BO**, and **3MeCz-BO**, respectively. Variations in distances and angles between the donor and acceptor units in the three compounds arise from the spatial effects of methyl groups. The measured D–A distances are as follows: D1 to A1 is 3.175 Å, D2 to A2 is 3.101 Å, and D3 to A3 is 3.192 Å. The dihedral angles of D1–A1, D2–A2, and D3–A3 are measured as 10.2°, 18.8°, and 14.7°, showing that they all have an aligned and parallel D–A spatial arrangement. This configuration can help enhance the radiative transitions of the compounds. The angle between D1 and the bridge is 84.4°, while those of D2–bridge and D3–bridge are 88.9° and 88.3°, respectively. Both D2 and D3 adopt nearly orthogonal conformations to the bridge, due to the locking effect of spiro-fluorene and the spatial hindrance of the methyl groups near the bridge. In contrast, D1, which has only one methyl group, forms a larger angle with the bridge, making it less conducive to the spatial alignment of D1 and A1. Due to the large steric hindrance imposed on the acceptors by the immobilized donor, the angles of A1, A2, and A3 relative to the bridge are measured to be 74.2°, 77.1°, and 73.6°, respectively. Nevertheless, they can still establish an effective face-to-face parallel arrangement between the donor and acceptor to ensure optimal π-orbital overlap. The observation of intramolecular noncovalent interactions is further corroborated by reduced density gradient (RDG) analysis.[41] The RDG iso-surfaces are colored on a blue-green-red scale based on

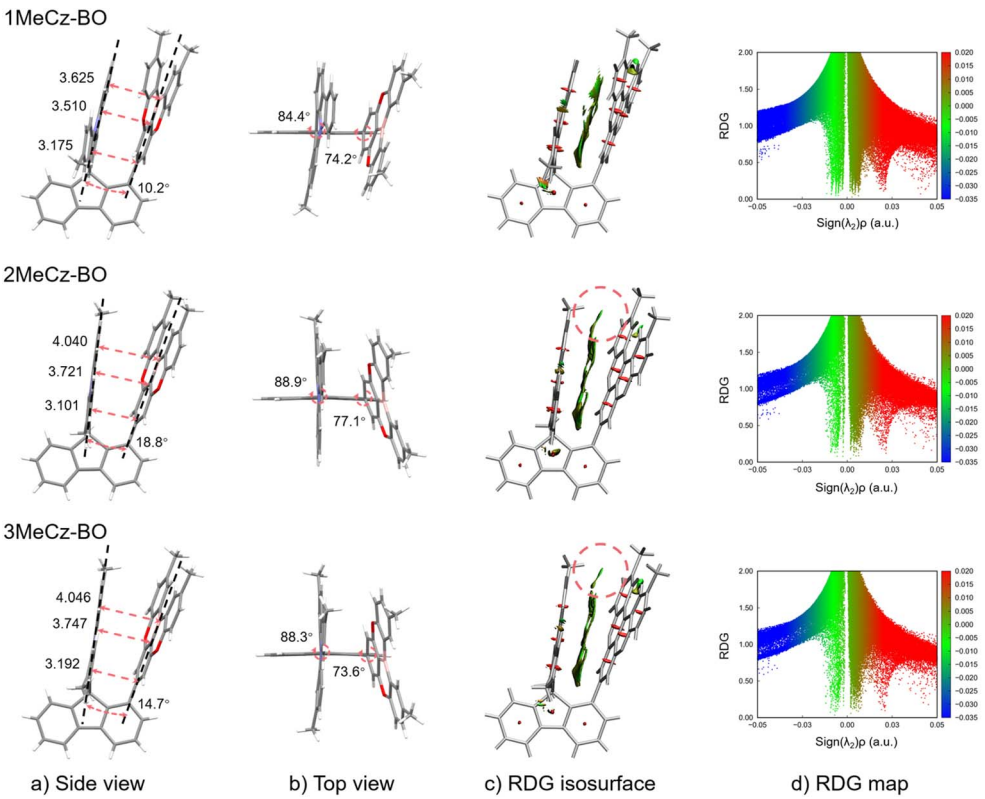

Fig. 2 (a) Side and (b) top views of the single crystal structures for **1MeCz-BO**, **2MeCz-BO**, and **3MeCz-BO**. The distribution of RDG isosurfaces (c) with the scatter plots of RDG *versus* sign(λ_2) (d).

the sign(λ_2)ρ, as shown in Fig. 2c. The iso-surfaces colored in green and brown between D and A units illustrate the π–π interactions and steric hindrance. For three compounds, large green and brown iso-surfaces are present between the donor and acceptor, suggesting significant π–π interactions that support the potential occurrence of the TSCT process. Furthermore, the steric hindrance between donor and acceptor units creates considerable rigidity, which restricts molecular vibrations and inhibits non-radiative transitions, leading to a narrow FWHM. In addition, in D2 and D3, the top methyl group introduces steric hindrance with the acceptors, as shown by the red dotted circle in Fig. 2c, which is not found between D1 and A1. This additional steric hindrance further dampen the vibration of the acceptor unit, which helps to further inhibit the process of non-radiative transition. According to the scatter diagrams of the RDG analysis (Fig. 2d), all three compounds show numerous and dense spikes in the green and brown regions, demonstrating the effective π–π interaction between the D and A units.

Density functional theory (DFT) and time-dependent density functional theory (TD-DFT) calculations were performed using the B3LYP-D3/6-31G(d) method to optimize the ground state configurations and analyze frontier molecular orbitals (FMOs) along with electron–hole distribution.[42] According to DFT simulations (Fig. S26†), we observed that the HOMO and LUMO mainly distribute on the donor and acceptor units, respectively, illustrating the ICT characteristics of the compounds. The HOMO energy levels were determined to be −5.01, −4.95, and −4.87 eV, while the LUMO energy levels were determined to be −1.45, −1.47, and −1.45 eV. Thus, the calculated E_g values of 3.56, 3.48, and 3.42 eV, for **1MeCz-BO**, **2MeCz-BO**, and **3MeCz-BO**, respectively, align well with the observed trend in electrochemical measurements. It was further confirmed that the ICTs improve progressively with more methyl groups on the donor. The rigidity of the molecules helps reduce the energy loss that occurs during structural relaxation. Therefore, **2MeCz-BO** and **3MeCz-BO** present similar radiative decay oscillator strengths (f) (0.0178 for **3MeCz-BO** and 0.0168 for **2MeCz-BO**), whereas **1MeCz-BO** shows an f of 0.0064, which is much lower than that of **3MeCz-BO** and **2MeCz-BO** owing to its relatively weaker structural rigidity and weaker ICT. Thus, the higher f will provide **3MeCz-BO** and **2MeCz-BO** with fast radiation transition rates.

The TD-DFT calculations show the excited-state energy levels, natural transition orbital (NTO) distributions, and CT proportion, as shown in Fig. 3. All three compounds exhibit CT-dominated S_1 states with 99.6% CT proportions. The energy levels of the S_1 states decrease slightly as the number of methyl groups in the donor unit increases, showing values of 2.998, 2.901, and 2.848 eV. This change occurs due to the enhancement of ICT caused by the additional electron-rich methyl groups in the donor. For **1MeCz-BO**, the weak ICT results in a large bandgap, leading to high energy levels for both the ^{1}CT and ^{3}CT. However, the ^{3}LE is mainly influenced by the molecular segment with the lowest energy, which is the acceptor unit. Thus, the T_1 of **1MeCz-BO** shows a 7.6% CT proportion and an energy level of 2.826 eV. Although the value of $\langle S_1|\hat{H}_{SOC}|T_1\rangle$ (0.393 cm^{-1}) is large, the large ΔE_{ST} (172 meV) makes the RISC process extremely difficult. In addition, **1MeCz-BO** exhibits a significant $\Delta E(^3CT - {}^3LE)$ (134 meV), making the RISC process inaccessible with the assistance of T_2. This suggests a slow RISC process for **1MeCz-BO**. For **2MeCz-BO**, the additional methyl group in the donor (compared to **1MeCz-BO**) can slightly decrease the energy level of ^{1}CT and ^{3}CT states, resulting in lower S_1 and T_2 (CT: 70.6%, 2.889 eV) energy levels than those of **1MeCz-BO**. However, the additional methyl groups in the donor have minimal impact on the ^{3}LE energy level, resulting in the T_1 (CT: 27.6%, 2.818 eV) of **2MeCz-BO** similar to that of **1MeCz-BO**. Thus the ΔE_{ST} of **2MeCz-BO** is significantly reduced to 83 meV. Furthermore, because of the distinct LE characteristics of T_1, a high value of $\langle S_1|\hat{H}_{SOC}|T_1\rangle$ of 0.330 cm^{-1} can be achieved, suggesting that an effective RISC process can occur from T_1 to S_1. In addition, the $\Delta E(^3CT - {}^3LE)$ (71 meV) of **2MeCz-BO** is also reduced, facilitating the mixing of ^{3}LE and ^{3}CT, as shown in Fig. 3d. Thus, the mixing of T_1 and T_2 allows the RISC process to be assisted by T_2. With the further addition of methyl groups, **3MeCz-BO** presents the lowest S_1, resulting in a minimized ΔE_{ST} of 51 meV. Additionally, the mixing of T_1 (CT: 63.8%, 2.797 eV) and T_2 (CT: 34.7%, 2.857 eV) is reinforced due

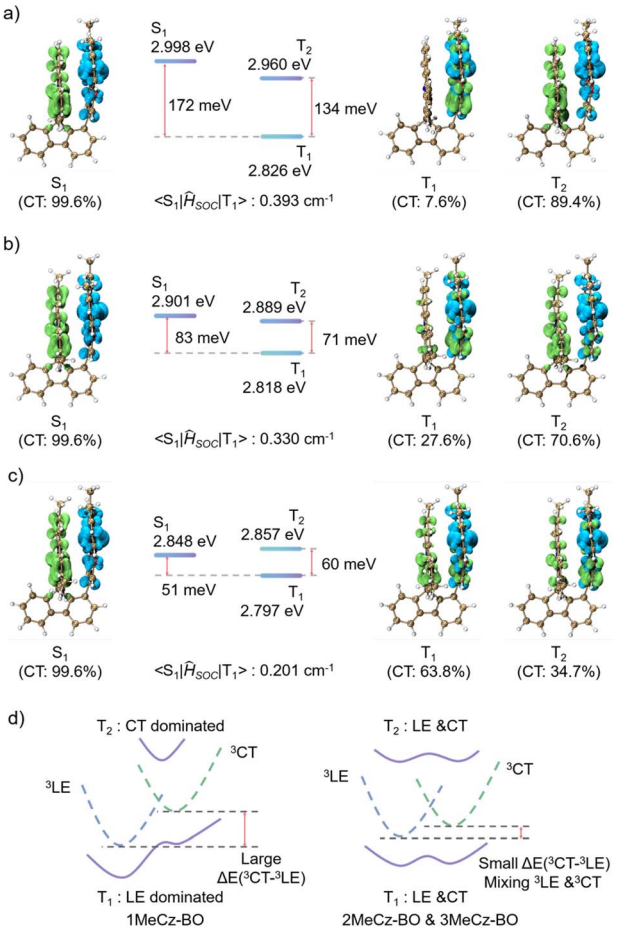

Fig. 3 Excited-state energy levels and natural transition orbital distributions for **1MeCz-BO** (a), **2MeCz-BO** (b), and **3MeCz-BO** (c). (d) Schematic diagram of interaction between ^{3}LE and ^{3}CT excited states.

to the further reduction of $\Delta E(^3CT - {}^3LE)$ (60 meV), suggesting more effective assistance from T_2. The smaller ΔE_{ST} with the high enough $\langle S_1|\hat{H}_{SOC}|T_1\rangle$ (0.201 cm^{-1}) ensures a faster RISC process of **3MeCz-BO**.

Photophysical properties

To investigate the photophysical properties of these emitters, UV-Vis absorption spectra, fluorescence spectra in dilute toluene solution (10^{-5} mol L^{-1}), and photoluminescence spectra in doped films were measured at 298 K, as shown in Fig. 4a. In the films, emitters (20 wt%) are doped in 10 wt% poly(*N*-vinylcarbazole) (PVK, $M_w \geq 50\,000$) and 70 wt% 1,3-bis(*N*-carbazolyl)benzene (mCP). As seen in the UV-Vis absorption spectra, all three emitters show two strong absorption bands at 280–320 nm and 340–410 nm. The band at 280–320 nm is attributed to the local π–π* transitions, and the band at 340–410 nm includes the characteristic absorption band of oxygen-bridged boron acceptor and ICT between D and A. The optical band-gap values are calculated from the onset of the absorption spectra, which are 3.00, 2.99, and 2.98 eV for **1MeCz-BO**, **2MeCz-BO**, and **3MeCz-BO**, respectively. The PL emission peaks in toluene solution are located at 416, 428, and 432 nm for **1MeCz-BO**, **2MeCz-BO**, and **3MeCz-BO**, with narrow FWHM values of 42, 41, and 39 nm, respectively. Compared to the PL emission in the toluene solution, the doped films exhibit more redshifted emission (423, 434, and 441 nm), and larger FWHM values (52, 51, and 49 nm). As expected, as the number of methyl groups in the donor increases, the emitters exhibit more redshifted emission, due to the electron-rich nature of the methyl groups. The fluorescence and phosphorescence spectra at 77 K in toluene were recorded to calculate the energy levels of S_1 and T_1 states, shown in Fig. 4b. The energy levels of S_1 states are determined to be 3.08, 3.01, and 2.95 eV, while the energy levels of T_1 states are determined to be 2.95, 2.95, 2.93 eV, for **1MeCz-BO**, **2MeCz-BO**, **3MeCz-BO**, respectively. The increase in the number of methyl groups in the donor is beneficial for improving the electron-donating ability of the donor, which in turn enhances the ICT process and reduces the energy level of the S_1 states with CT characteristics. By contrast, these three emitters have similar T_1 energy levels, since T_1 states are mainly distributed on the same acceptor units. In particular, because the T_1 state of **3MeCz-BO** exhibits more CT characteristics, it shows a relatively low T_1 energy level. Therefore, the corresponding ΔE_{ST}s of **1MeCz-BO**, **2MeCz-BO**, and **3MeCz-BO** are calculated to be 0.13, 0.06, and 0.02 eV, respectively. **3MeCz-BO** shows extremely small ΔE_{ST}, leading to the most effective RISC process. Fig. 4c illustrates the PL spectra of three emitters in different solvents at 298 K, showing obvious solvatochromism and highlighting the distinct CT characteristics of the S_1 states.

To investigate the TADF properties of these emitters, the transient photoluminescence decay curves of the doped films in air and in a vacuum were measured, as shown in Fig. 4d (for **3MeCz-BO**) and Fig. S27† (for **1MeCz-BO** and **2MeCz-BO**). They show noticeable delayed fluorescence and display a clear difference between the decay curves in a vacuum and in air, confirming that triplet excitons are involved in delayed fluorescence processes. Fig. S28† shows the decay curves over a larger range. Then the temperature-dependent transient PL decay spectra of the three emitters were measured in the doped films, as shown in Fig. 4e (for **3MeCz-BO**) and Fig. S29† (for **1MeCz-BO** and **2MeCz-BO**). The enhanced lifetimes and proportions of delayed fluorescence as the temperature

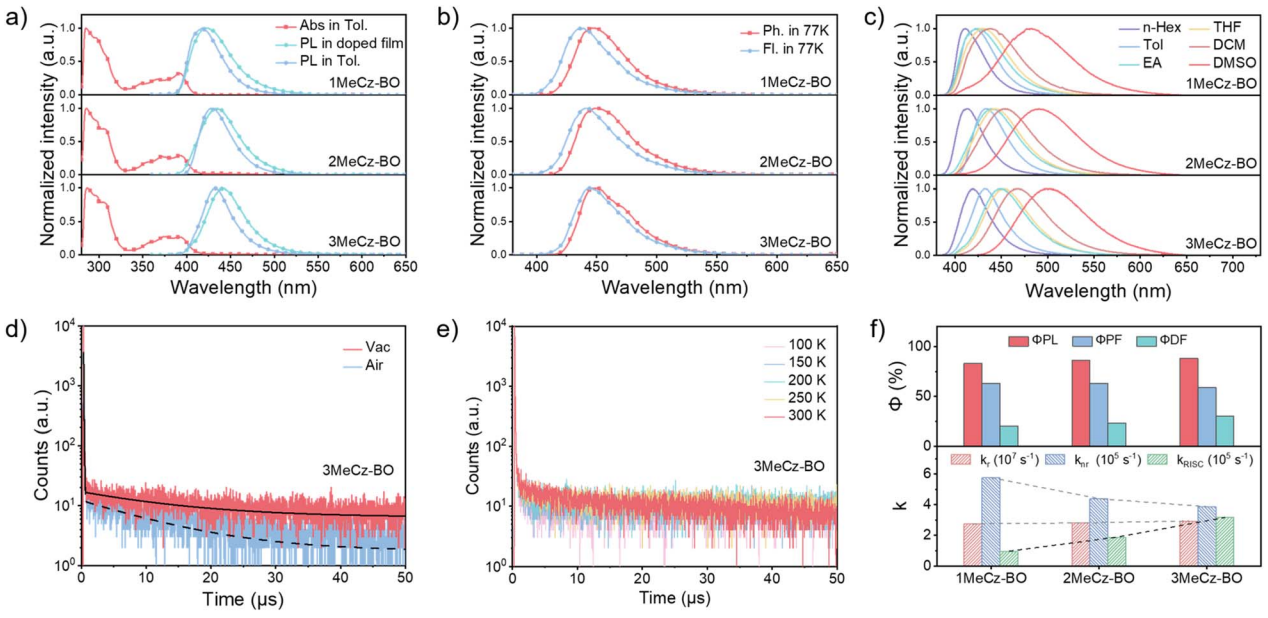

Fig. 4 (a) The UV-Vis absorption and fluorescence spectra in toluene (10^{-5} mol L^{-1}, 298 K), and photoluminescence spectra in the doped films. (b) The fluorescence and phosphorescence spectra at 77 K in toluene (10^{-5} mol L^{-1}). (c) The photoluminescence spectra in different solvents at 298 K. (d) The transient photoluminescence decay curves of the doped films in air and in a vacuum for **3MeCz-BO**. (e) The temperature-dependent transient photoluminescence decay spectra of **3MeCz-BO**. (f) Comparison of the efficiencies (ϕ) of PL, PF, DF, and the rate constants (k) of radiation, non-radiation, and RISC.

Table 1 Photophysical properties of **1MeCz-BO**, **2MeCz-BO**, and **3MeCz-BO**

Compound	λ_{PL}[a] [nm]	FWHM[b] [nm]	S_1/T_1[c] [eV]	ΔE_{ST}[d] [eV]	HOMO/LUMO[e] [eV]	E_g[f] [eV]	PLQY[g] [%]	k_r[h] [10^7 s^{-1}]	k_{RISC}[i] [10^5 s^{-1}]
1MeCz-BO	416, 423	42, 52	3.08/2.95	0.13	−5.41/−2.85	2.56	83	2.75	0.95
2MeCz-BO	428, 434	41, 51	3.01/2.95	0.06	−5.29/−2.84	2.45	86	2.81	1.87
3MeCz-BO	432, 441	39, 49	2.95/2.93	0.02	−5.23/−2.82	2.41	88	2.92	3.17

[a] The photoluminescence spectra in toluene (10^{-5} M) solution and doped films at 298 K. [b] The full-width-at-half maximum of PL spectra in toluene solution and doped films. [c] Determined from the onset of fluorescence and phosphorescence spectra in toluene solution at 77 K. [d] $\Delta E_{ST} = S_1 - T_1$. [e] Estimated from the oxidation and redox potential in cyclic voltammetry. [f] The energy gap (E_g) values calculated from the HOMO–LUMO levels. [g] The photoluminescence quantum yields of doped films in a vacuum. [h] The radiative rate constants. [i] The rate constants of reverse intersystem crossing.

increases from 100 to 300 K further confirm the thermally activated mechanism of the three emitters. It can be seen that temperature has the greatest effect on the decay curve of **1MeCz-BO**, followed by **2MeCz-BO** with the least impact observed for **3MeCz-BO**. This phenomenon is closely related to their ΔE_{ST}-values. For **1MeCz-BO**, **2MeCz-BO**, and **3MeCz-BO** films, the prompt lifetimes (τ_p) are measured as 22.9, 22.5, and 20.2 ns, while the delayed lifetime (τ_d) are measured as 14.1, 7.32, and 4.73 μs, respectively. Furthermore, the photoluminescence quantum yields (PLQYs) of doped films were measured in a vacuum (by converting the PLQYs of doped films in air, using the integral ratio of the steady-state emissions of the corresponding films in a vacuum to those in air). **1MeCz-BO**, **2MeCz-BO** and **3MeCz-BO** display PLQYs of 83%, 86%, and 88%, respectively. All three compounds exhibit the highest PLQY at a doping ratio of 20 wt%, which may be attributed to the formation of rigid π-stacked structures[17] (Fig. S30†). To quantitatively compare the exciton kinetics of the emitters, the rate constants of radiation (k_r), non-radiation (k_{nr}), and RISC (k_{RISC}) (Fig. 4f) were precisely calculated according to a previously reported method.[43] The k_r values for **1MeCz-BO**, **2MeCz-BO** and **3MeCz-BO** are 2.75×10^7, 2.81×10^7, and 2.92×10^7 s^{-1}, respectively. High k_r values demonstrate the face-to-face D–A arrangements and short D–A distances. Meanwhile, the k_{RISC} values of **1MeCz-BO**, **2MeCz-BO**, and **3MeCz-BO** are measured to be 9.5×10^4, 1.87×10^5, and 3.17×10^5 s^{-1}, respectively. With the modification of methyl groups, the RISC rate gradually increases, which is consistent with the results obtained by the NTO analysis. Moreover, the values of k_{nr} have been calculated to be 5.75×10^6, 4.38×10^6, and 3.87×10^6 s^{-1} for **1MeCz-BO**, **2MeCz-BO**, and **3MeCz-BO**, respectively. It has been demonstrated that the increased molecular rigidity from the methyl groups can inhibit non-radiative transitions. The photophysical data of three emitters are given in Tables 1 and S5.†

Electroluminescence properties

Promised by the minimized ΔE_{ST} and enhanced RISC process of the ultra-deep-blue emitter **3MeCz-BO**, the corresponding OLED devices were fabricated to investigate the electroluminescence (EL) performances of the emitters with the following structure: ITO/PEDOT:PSS (30 nm)/PVK (10 nm)/mCP: 20 wt% emitters and 10 wt% PVK (40 nm)/DPEPO (5 nm)/TmPyPB (35 nm)/LiF

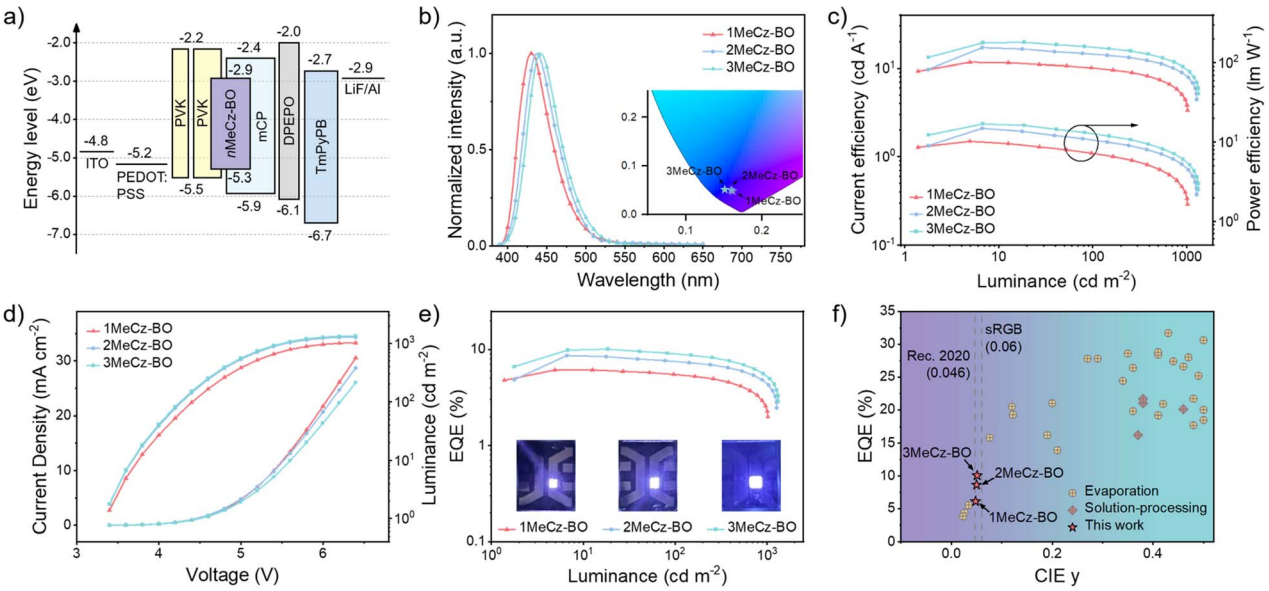

Fig. 5 (a) Device architecture and energy levels of the used materials. (b) EL spectra of **1MeCz-BO**-, **2MeCz-BO**-, and **3MeCz-BO**-based OLEDs. (c) Current efficiency and power efficiency *versus* luminance of the devices. (d) Current density–voltage–luminance (*J*–*V*–*L*) characteristics of the devices. (e) EQE *versus* luminance of the devices. (f) EQE_{max}s with CIE_y obtained in this work and the reported TSCT-TADF emitters (CIE_y < 0.5).

Table 2 Summary of electroluminescence performances

Materials	λ_{EL}[a] [nm]	EQE_{max}[b] [%]	EQE_{100}[c] [%]	EQE_{500}[d] [%]	CE_{max}[e] [cd A^{-1}]	PE_{max}[f] [lm W^{-1}]	L_{max}[g] [cd m^{-2}]	FWHM[h] [nm]	CIE[i] [x, y]
1MeCz-BO	430	6.1	5.5	4.2	11.7	10.2	1024	49	0.162, 0.048
2MeCz-BO	436	8.6	7.5	6.0	17.1	14.9	1277	49	0.160, 0.050
3MeCz-BO	442	10.1	9.0	7.1	19.6	16.9	1334	50	0.151, 0.051

[a] The peak value of electroluminescence. [b] Maximum external quantum efficiency. [c] External quantum efficiency at 100 cd m^{-2}. [d] External quantum efficiency at 500 cd m^{-2}. [e] Maximum current efficiency. [f] Maximum power efficiency. [g] Maximum luminance. [h] Full width at half-maximum of the electroluminescence peak. [i] Coordinates of Commission Internationale de L'Eclairage.

(0.8 nm)/Al (100 nm). Poly(3,4-ethylenedioxythiophene):poly(styrenesulfonate) (PEDOT:PSS) was used as the hole-injection and hole-transporting layer, lithium fluoride (LiF) was used as the electron-injection layer, and 1,3,5-tri[(3-pyridyl)-phen-3-yl] benzene (TmPyPB) was used as the electron-transporting layer. PVK and bis[2-(diphenylphosphino) phenyl]ether oxide (DPEPO) were used as the electron- and hole-blocking layers, respectively, while mCP was used as the host material. "*n*MeCz-BO" refers to the series of these emitters: **1MeCz-BO**, **2MeCz-BO**, and **3MeCz-BO**. The energy level diagram of the materials used in OLEDs is shown in Fig. 5a, and the EL properties are summarized in Table 2. The EL properties at other doping ratios are shown in Fig. S31–S33 and Tables S6–S8.†

For three emitters, the highest efficiency of devices can be obtained at a doped ratio of 20 wt%. Devices based on **1MeCz-BO**, **2MeCz-BO**, and **3MeCz-BO** display EL peaks (λ_{EL}) at 430, 436, and 442 nm with FWHM values of 49, 49, and 50 nm, respectively (Fig. 5b). The corresponding CIE coordinates show ultra-deep-blue colors of (0.162, 0.048), (0.160, 0.050), and (0.151, 0.051) for **1MeCz-BO**, **2MeCz-BO**, and **3MeCz-BO**, respectively. The emissions from these devices show a slight redshift as the number of methyl groups in the donor increases, which is consistent with the results of molecular simulations and photophysics. All three solution-processed devices exhibit narrow emission, which aligns with the measured FWHM values in photophysics. The rigid molecular structures effectively reduce vibrational relaxation, leading to narrow emissions. This is advantageous for the color purity of ultra-deep-blue OLEDs.

Furthermore, the CIE coordinates of **1MeCz-BO** and **2MeCz-BO** are (0.162, 0.048) and (0.160, 0.050), respectively, exhibiting more violet emission. While the CIE coordinates of **3MeCz-BO** (0.151, 0.051) fit well within the sRGB of CIE (0.15, 0.06), and are close to the CIE (0.131, 0.046) for the Rec. 2020 standard. This suggests its potential application in colorful display devices. As shown in Fig. 5c, the current efficiencies (CEs) of **1MeCz-BO**, **2MeCz-BO**, and **3MeCz-BO**-based OLEDs are 11.7, 17.1, and 19.6 cd A^{-1}, respectively. Their power efficiencies (PEs) are 10.2, 14.9, and 16.9 lm W^{-1}. This suggests that the enhanced electrical properties of the emitters are due to the methyl-modification. In terms of device performance, **3MeCz-BO** exhibits a maximum EQE of 10.1%, which is higher than that of **2MeCz-BO** (8.6%) and **1MeCz-BO** (6.1%). The EQEs at 100 cd m^{-2} are 5.5%, 7.5%, and 9.0%, and the EQEs at 500 cd m^{-2} are 4.2%, 6.0%, and 7.1% for **1MeCz-BO**, **2MeCz-BO**, and **3MeCz-BO**, respectively, showing the suppressed efficiency roll-offs. Additionally, the maximum luminance of the devices is measured as 1024, 1277, and 1334 cd m^{-2}, indicating that these devices exhibit high brightness as ultra-deep-blue solution-processing OLEDs. The criss-crossed stacking structures (Fig. S22†) prevent triplet–triplet annihilation of the materials, leading to the highest EQE at relatively high doping ratios (20 wt%). The high concentration of emitters provides higher brightness for the OLEDs, which is particularly challenging for ultra-deep-blue or deep-blue solution-processed OLEDs. These results indicate that the methyl groups on the donor suppress the non-radiative transitions and the enhanced ITC accelerates the RISC, thereby significantly enhancing the device performance of ultra-deep-blue TSCT materials. A summary of device data for face-to-face TSCT-TADF emitters (CIE_y < 0.5) is shown in Fig. 5f.[8–27] It can be seen that this work fills the gap in the violet to deep blue region of TSCT materials. For comparison, thermal evaporated OLEDs based on **3MeCz-BO** were also tested, as shown in Fig S34 and Table S9.† As a solution-processed device, it does not demonstrate significant disadvantages compared to the thermally evaporated device. Additionally, the limited broadening in the EL spectrum (compared to the PL in doped films) indicates the potential use of these materials in narrowband ultra-deep-blue OLEDs.

Conclusions

In summary, we proposed a strategy of methyl-modification in the donor to enhance the ICT and accelerate the RISC process of ultra-deep-blue TSCT-TADF emitters, solving the challenging issue of large ΔE_{ST} values and low k_{RISC} values in these materials. Due to the electron-rich nature of methyl groups, the ICT was enhanced and the energy levels of the ^{1}CT and ^{3}CT states were reduced, while the ^{3}LE remains unaffected by the methyl group. In this way, the ΔE_{ST} and $\Delta E(^3\text{CT} - {}^3\text{LE})$ of the materials can be minimized. This enables effective RISC processes from T_1 to S_1, which can be accelerated with the assistance of T_2. The prepared emitters **1MeCz-BO**, **2MeCz-BO**, and **3MeCz-BO** display k_{RISC} values of 9.5×10^4, 1.87×10^5, and 3.17×10^5 s^{-1}, respectively. In addition, ultra-deep-blue solution-processed OLED devices based on these materials exhibit good overall performance. The EQE_{max} of **3MeCz-BO** is 10.1%, with CIE coordinates of (0.151, 0.051) and a high luminance of 1334 cd m^{-2}. This work developed the first high-performance ultra-deep-blue solution-processed TSCT-TADF OLEDs. Additionally, their colour fits well within the sRGB of CIE coordinates of

(0.15, 0.06), and is close to the CIE coordinates of (0.131, 0.046) for the Rec. 2020 standard.

Data availability

The experimental procedures, characterization data, crystals data and device data generated in this study are provided in the ESI.†

Author contributions

Z. Ren and Q. Li designed the experiments. Q. Li synthesized the molecules, carried out the photophysical measurements and theoretical calculations, fabricated OLEDs and wrote the manuscript draft. H. Zhao and J. Zhao helped fabricate the OLEDs. Z. Cao and C. Yu helped synthesize the molecules. S. Yan and Z. Ren wrote the manuscript and supervised this study.

Conflicts of interest

There is no conflict of interest to report.

Acknowledgements

The authors acknowledge the financial support from the National Natural Science Foundation of China (No. 52273164) and the Shandong Provincial Natural Science Foundation (ZR2022ZD37).

Notes and references

1 H. Uoyama, K. Goushi, K. Shizu, H. Nomura and C. Adachi, Highly efficient organic light-emitting diodes from delayed fluorescence, *Nature*, 2012, **492**, 234–238.
2 Y. Liu, C. Li, Z. Ren, S. Yan and M. R. Bryce, All-organic thermally activated delayed fluorescence materials for organic light-emitting diodes, *Nat. Rev. Mater.*, 2018, **3**, 18020.
3 G. Hong, X. Gan, C. Leonhardt, Z. Zhang, J. Seibert, J. M. Busch and S. Brase, A brief history of oleds-emitter development and industry milestones, *Adv. Mater.*, 2021, **33**, e2005630.
4 S. Shao, J. Hu, X. Wang, L. Wang, X. Jing and F. Wang, Blue thermally activated delayed fluorescence polymers with nonconjugated backbone and through-space charge transfer effect, *J. Am. Chem. Soc.*, 2017, **139**, 17739–17742.
5 H. Tsujimoto, D.-G. Ha, G. Markopoulos, H. S. Chae, M. A. Baldo and T. M. Swager, Thermally activated delayed fluorescence and aggregation induced emission with through-space charge transfer, *J. Am. Chem. Soc.*, 2017, **139**, 4894–4900.
6 Q. Xue and G. Xie, Thermally activated delayed fluorescence beyond through-bond charge transfer for high-performance OLEDs, *Adv. Opt. Mater.*, 2021, **9**, 2002204.
7 T. Zhang, Y. Xiao, H. Wang, S. Kong, R. Huang, V. Ka-Man Au, T. Yu and W. Huang, Highly twisted thermally activated delayed fluorescence (TADF) molecules and their applications in organic light-emitting diodes (OLEDs), *Angew. Chem.*, 2023, **62**, e202301896.
8 X. Tang, L. S. Cui, H. C. Li, A. J. Gillett, F. Auras, Y. K. Qu, C. Zhong, S. T. E. Jones, Z. Q. Jiang, R. H. Friend and L. S. Liao, Highly efficient luminescence from space-confined charge-transfer emitters, *Nat. Mater.*, 2020, **19**, 1332–1338.
9 Y. Wada, H. Nakagawa, S. Matsumoto, Y. Wakisaka and H. Kaji, Organic light emitters exhibiting very fast reverse intersystem crossing, *Nat. Photonics*, 2020, **14**, 643–649.
10 S.-Y. Yang, Q.-S. Tian, Y.-J. Yu, S.-N. Zou, H.-C. Li, A. Khan, Q.-H. Wu, Z.-Q. Jiang and L.-S. Liao, Sky-blue thermally activated delayed fluorescence with intramolecular spatial charge transfer based on a dibenzothiophene sulfone emitter, *J. Org. Chem.*, 2020, **85**, 10628–10637.
11 T.-T. Wang, G. Xie, H.-C. Li, S.-Y. Yang, H. Li, Y.-L. Xiao, C. Zhong, K. Sarvendra, A. Khan, Z.-Q. Jiang and L.-S. Liao, π-stacked thermally activated delayed fluorescence emitters with alkyl chain modulation, *CCS Chem.*, 2021, **3**, 1757–1763.
12 T. Huang, Q. Wang, G. Meng, L. Duan and D. Zhang, Accelerating radiative decay in blue through-space charge transfer emitters by minimizing the face-to-face donor-acceptor distances, *Angew. Chem.*, 2022, **61**, e202200059.
13 Z. Zhao, C. Zeng, X. Peng, Y. Liu, H. Zhao, L. Hua, S. J. Su, S. Yan and Z. Ren, Tuning intramolecular stacking of rigid heteroaromatic compounds for high-efficiency deep-blue through-space charge-transfer emission, *Angew. Chem., Int. Ed.*, 2022, **61**, e202210864.
14 Q. Li, Z. Zhao, H. Zhao, Y. Guo, X. Tong, S. Yan and Z. Ren, Enhancing light-emitting efficiency of blue through-space charge transfer emitters via fixing configuration induced by intramolecular hydrogen bonding, *ACS Appl. Mater. Interfaces*, 2024, **16**, 22238–22247.
15 Y. K. Qu, D. Y. Zhou, Q. Zheng, P. Zuo, Z. L. Che, L. S. Liao and Z. Q. Jiang, Linearly arranged multi-π-stacked structure for efficient through-space charge-transfer emitters, *Angew. Chem., Int. Ed.*, 2024, **63**, e202408712.
16 P. Zuo, Y. J. Yang, F. M. Liu, J. R. Wu, Q. Zheng, H. T. Yuan, L. S. Liao, D. Y. Zhou and Z. Q. Jiang, Achieving deep-blue through-space charge-transfer emitter by designing the donor-π-donor-σ-acceptor molecular structure, *Adv. Opt. Mater.*, 2024, **12**, 2400860.
17 S. Y. Yang, Z. Q. Feng, Z. Fu, K. Zhang, S. Chen, Y. J. Yu, B. Zou, K. Wang, L. S. Liao and Z. Q. Jiang, Highly efficient sky-blue π-stacked thermally activated delayed fluorescence emitter with multi-stimulus response properties, *Angew. Chem., Int. Ed.*, 2022, **61**, e202206861.
18 C. C. Peng, S. Y. Yang, H. C. Li, G. H. Xie, L. S. Cui, S. N. Zou, C. Poriel, Z. Q. Jiang and L. S. Liao, Highly efficient thermally activated delayed fluorescence via an unconjugated donor-acceptor system realizing EQE of over 30%, *Adv. Mater.*, 2020, **32**, e2003885.
19 S. Y. Yang, Y. K. Wang, C. C. Peng, Z. G. Wu, S. Yuan, Y. J. Yu, H. Li, T. T. Wang, H. C. Li, Y. X. Zheng, Z. Q. Jiang and L. S. Liao, Circularly polarized thermally activated delayed fluorescence emitters in through-space charge transfer on

asymmetric spiro skeletons, *J. Am. Chem. Soc.*, 2020, **142**, 17756–17765.

20 Y. Song, M. Tian, R. Yu and L. He, Through-space charge-transfer emitters developed by fixing the acceptor for high-efficiency thermally activated delayed fluorescence, *ACS Appl. Mater. Interfaces*, 2021, **13**, 60269–60278.

21 X. Q. Wang, S. Y. Yang, Q. S. Tian, C. Zhong, Y. K. Qu, Y. J. Yu, Z. Q. Jiang and L. S. Liao, Multi-layer π-stacked molecules as efficient thermally activated delayed fluorescence emitters, *Angew. Chem., Int. Ed.*, 2021, **60**, 5213–5219.

22 Z. Q. Feng, S. Y. Yang, F. C. Kong, Y. K. Qu, X. Y. Meng, Y. J. Yu, D. Y. Zhou, Z. Q. Jiang and L. S. Liao, Indirect control of donor/acceptor interactions for highly efficient space-confined thermally activated delayed fluorescence emitters, *Adv. Funct. Mater.*, 2022, **33**, 2209708.

23 F. M. Xie, H. Z. Li, K. Zhang, Y. Shen, X. Zhao, Y. Q. Li and J. X. Tang, A dislocated twin-locking acceptor-donor-acceptor configuration for efficient delayed fluorescence with multiple through-space charge transfer, *Angew. Chem., Int. Ed.*, 2022, **61**, e202213823.

24 J. Liu, Z. Feng, C. Peng, Y. Yu, S. Yang, Z. Jiang and L. Liao, Acceptor modulation for improving thermally activated delayed fluorescence emitter in through-space charge transfer on spiroskeletons, *Chin. Chem. Lett.*, 2023, **34**, 107634.

25 Y. Song, K. Zhang, P. Wang, Y. Cao and L. He, Simultaneously improving radiative decay and reverse intersystem crossing in space-confined through-space, *Adv. Funct. Mater.*, 2024, 2411957.

26 X. Lan, J. Zeng, J. Chen, T. Yang, X. Dong, B. Z. Tang and Z. Zhao, Robust sandwich-structured thermally activated delayed fluorescence molecules utilizing 11,12-dihydroindolo[2,3-a]carbazole as bridge, *Angew. Chem., Int. Ed.*, 2024, e202414488.

27 H.-T. Yuan, Z.-H. Qu, P. Zuo, Y.-J. Yang, Q. Zheng, F.-M. Liu, M.-T. Li, L.-S. Liao and Z.-Q. Jiang, Comparative study on two kinds of spiro systems for constructing through-space charge-transfer emitters, *J. Phys. Chem. C*, 2024, **128**, 14538–14545.

28 C. Jiang, J. Miao, D. Zhang, Z. Wen, C. Yang and K. Li, Acceptor-donor-acceptor π-stacking boosts intramolecular through-space charge transfer towards efficient red TADF and high-performance OLEDs, *Research*, 2022, **2022**, 9892802.

29 X. F. Song, C. Jiang, N. Li, J. Miao, K. Li and C. Yang, Simultaneously enhancing the planarity and electron-donating capability of donors for through-space charge transfer TADF towards deep-red emission, *Chem. Sci.*, 2023, **14**, 12246–12254.

30 Y.-J. Yu, M. Song, X.-Y. Meng, Y.-K. Qu, X.-Q. Wang, L. Chen, S.-Y. Yang, D.-Y. Zhou, Z.-Q. Jiang and L.-S. Liao, Design and synthesis of red through-space charge transfer thermally activated delayed fluorescence emitters with donor/acceptor/donor stacking, *Org. Lett.*, 2023, **25**, 6024–6028.

31 P. Chen, C. Jiang, N. Li, X.-F. Song, X. Wan, H. Liu, J.-G. Yang and K. Li, Sandwich-type thermally activated delayed fluorescence molecules with through-space charge transfer excited state for red OLEDs, *Org. Electron.*, 2024, **133**, 107114.

32 H. Hirai, K. Nakajima, S. Nakatsuka, K. Shiren, J. Ni, S. Nomura, T. Ikuta and T. Hatakeyama, One-step borylation of 1,3-diaryloxybenzenes towards efficient materials for organic light-emitting diodes, *Angew. Chem., Int. Ed.*, 2015, **54**, 13581–13585.

33 D. H. Ahn, S. W. Kim, H. Lee, I. J. Ko, D. Karthik, J. Y. Lee and J. H. Kwon, Highly efficient blue thermally activated delayed fluorescence emitters based on symmetrical and rigid oxygen-bridged boron acceptors, *Nat. Photonics*, 2019, **13**, 540–546.

34 T. Hua, X. Cao, J. Miao, X. Yin, Z. Chen, Z. Huang and C. Yang, Deep-blue organic light-emitting diodes for ultrahigh-definition displays, *Nat. Photonics*, 2024, **18**, 1161–1169.

35 J. Ochi, Y. Yamasaki, K. Tanaka, Y. Kondo, K. Isayama, S. Oda, M. Kondo and T. Hatakeyama, Highly efficient multi-resonance thermally activated delayed fluorescence material toward a BT.2020 deep-blue emitter, *Nat. Commun.*, 2024, **15**, 2361.

36 R. W. Weerasinghe, S. Madayanad Suresh, D. Hall, T. Matulaitis, A. M. Z. Slawin, S. Warriner, Y. T. Lee, C. Y. Chan, Y. Tsuchiya, E. Zysman-Colman and C. Adachi, A boron, nitrogen, and oxygen doped π-extended helical pure blue multiresonant thermally activated delayed fluorescent emitter for organic light emitting diodes that shows fast k_{RISC} without the use of heavy atoms, *Adv. Mater.*, 2024, **36**, e2402289.

37 T. Yang, N. Qiu, X. Lan, X. Dong, B. Z. Tang and Z. Zhao, Efficient folded molecules with intramolecular through-space charge transfer for near-ultraviolet organic light-emitting diodes, *J. Phys. Chem. C*, 2024, **128**, 16085–16092.

38 Q. Zhang, J. Li, K. Shizu, S. Huang, S. Hirata, H. Miyazaki and C. Adachi, Design of efficient thermally activated delayed fluorescence materials for pure blue organic light emitting diodes, *J. Am. Chem. Soc.*, 2012, **134**, 14706–14709.

39 Q. Zhang, B. Li, S. Huang, H. Nomura, H. Tanaka and C. Adachi, Efficient blue organic light-emitting diodes employing thermally activated delayed fluorescence, *Nat. Photonics*, 2014, **8**, 326–332.

40 X. Cai and S. J. Su, Marching toward highly efficient, pure-blue, and stable thermally activated delayed fluorescent organic light-emitting diodes, *Adv. Funct. Mater.*, 2018, **28**, 1802558.

41 T. Lu and F. Chen, Multiwfn: a multifunctional wavefunction analyzer, *J. Comput. Chem.*, 2012, **33**, 580–592.

42 S. Grimme, S. Ehrlich and L. Goerigk, Effect of the damping function in dispersion corrected density functional theory, *J. Comput. Chem.*, 2011, **32**, 1456–1465.

43 K. Masui, H. Nakanotani and C. Adachi, Analysis of exciton annihilation in high-efficiency sky-blue organic light-emitting diodes with thermally activated delayed fluorescence, *Org. Electron.*, 2013, **14**, 2721–2726.